Fabrication of low-dimensional microstructures with distyrylbenzene derivatives

Tomoya Akazawa[1], Fumio Sasaki[2], Kazuki Bando[3], Hitoshi Mizuno[1]*, Hiroyuki Katsuki[1], and Hisao Yanagi[1]*

[1] *Graduate School of Science and Technology, Nara Institute of Science and Technology (NAIST), 8916-5 Takayama, Ikoma, Nara 630-0192, Japan*

[2] *Electronics and Photonics Research Institute, National Institute of Advanced Industrial Science and Technology (AIST), 1-1-1 Umezono, Tsukuba, Ibaraki 305-8568, Japan*

[3] *Department of Physics, Faculty of Science, Shizuoka University, 836 Ohya, Suruga-ku, Shizuoka 422-8529, Japan*

E-mail: hitoshi352-17@ms.naist.jp, yanagi@ms.naist.jp

Microneedle crystals of 1,4-bis-(4-methylstyryl)benzene (DSB-4Me) and amorphous microdots of bis (*N*,*N*-di-*p*-tolylamino-*p*-styryl)benzene (DADSB) are fabricated by using mask-shadowing and conventional vapor deposition techniques. By interaction between π-conjugated electronic chains and ionic lattice of a KCl crystal substrate, DSB-4Me molecules grow into needle crystals epitaxially orienting in four directions making ±60° against $[110]_{KCl}$ and $[-110]_{KCl}$. As for DADSB, self-assembly into microdots by heating the KCl substrate at 180°C during deposition is attributed to the impact of bulky peripheral groups in DADSB and surface migration of the deposited molecules. Moreover, while amplified spontaneous emission (ASE) is observed above an excitation threshold of 362 μJ/cm^2 in the DSB-4Me microneedle crystals, a lower threshold whispering-gallery mode (WGM) lasing is observed above 37 μJ/cm^2 for DADSB microdots owing to the higher waveguide quality.

1. Introduction

Miniaturization of lasers is of major interest for photonic and optoelectronic devices such as all-optical computing and biomedical imaging.[1-8] Semiconductor lasers with micro- and nanostructures are building blocks for their devices.[4-6, 9-11] In comparison to inorganic materials, organic materials have advantages, such as compatibility with plastic substrates, tunable emission wavelengths at the visible region, low-cost, and low-temperature processing. Among organic devices, the organic lasers have currently lied at the heart of the interests owing to an observation of current-injection lasing from an organic light-emitting diode structure reported by Adachi *et al*.[3] To observe the lasing, fabrication of a microresonator which is formed by the facets of crystals with micrometer sizes with regular shapes is essential.[4-6, 9-11]

However, fabrication methods of organic crystals with regular shapes have not yet been fully established.[10-24] There are reports on patterned thiophene/phenylene co-oligomer (TPCO) single-crystalline microcavity array using lithography techniques.[14, 15, 19] In the lithography and dry etching, there is a concern on the damage incurring during reactive ion etching (RIE) for organic crystals, in addition to many fabrication steps. Although there are reports on self-assembled crystals[13, 16-21] with well-shaped side facets fabricated by solution processes, the control of the dimensions, sizes, and shape of microstructures is of great importance in observing the lasing. Meanwhile, epitaxial self-assembly of organic molecules is one of the unique fabrication methods for microstructures such as one-dimensional microneedles and microdots,[11, 22, 23] in terms of fewer fabrication processes and a capable of shape control of microresonators through the interaction between the molecules and a substrate. Herein, we report on the fabrication of microneedle crystals and microdots on ionic crystal substrates using distyrylbenzene derivatives that exhibit excellent lasing performances.[22-28] The light amplification characteristics of these microstructures are also demonstrated to verify the utility as gain media.

2. Experimental methods

1,4-bis-(4-methylstyryl)benzene (DSB-4Me) and bis (*N*,*N*-di-*p*-tolylamino-*p*-styryl)benzene (DADSB) were purchased from Tokyo Kasei Kogyo (Tokyo, Japan). DSB-4Me was purified by vacuum sublimation once before use. For fabrication of DSB-4Me microneedle crystals, we used a mask-shadowing vapor-deposition technique[30] which enables the growth of self-waveguiding crystals only on the masked regions (pinhole diameter: 0.6 mm, hole spacing: 1.1 mm) on a cleaved (001) face of a potassium chloride

(KCl) single-crystal substrate. The KCl single crystal was cleaved to provide the substrate ($10\times10\times1$ mm^3) in air, and the substrate was transferred immediately into a vacuum chamber (pressure: 2×10^{-4} Pa). When the substrate temperature (T_s) reaches T_s=70°C or 100°C during deposition, the DSB-4Me was vapor-deposited onto the KCl (001) surface at a deposition rate of 0.23 Å/s or 0.9 Å/s, respectively. For fabrication of microdots, DADSB was vacuum-deposited at a rate of more than 2.0 Å/s on the KCl substrate kept at T_s=180°C that induces a molecular migration on the surface and nucleation at the steps and kink sites existing on the (001) terrace. To prevent photo-oxidative degradation of DADSB molecules upon high-density photoexcitation, the deposited microdots on the KCl substrate were covered with a cap layer composed of MgF_2. The fluorescence images of DSB-4Me microneedle crystals and DADSB microdots were taken under excitation at λ_{ex} = 365 nm (Olympus BX51). For preparation of a sample for x-ray diffraction (XRD) measurements, amorphous carbon was deposited by thermal evaporation on the DSB-4Me microneedle crystals or DADSB microdots grown on the KCl substrates. Then, we used ultrapure water to dissolve the KCl substrates, thereby allowing the DSB-4Me microneedles or DADSB microdots to be transferred onto a glass substrate. To determine the crystal structure of DSB-4Me, platelet-like single crystals were prefabricated by solution-grown method.[20, 21] 3.8 mg of DSB-4Me powder was dissolved in a mixed solvent (12 g) of toluene and hexane (1:1 volume ratio) at 80°C, and then crystals were precipitated by gradually cooling the solvent to 30°C in more than 12 hours. By filtrating the resulting solution, we obtained the single crystals for XRD measurements. The XRD measurements of the DSB-4Me microneedle crystals and DADSB microdots were carried out using a RINT-TTRIII/NM (Rigaku). The Mo-Kα radiation (λ = 0.71075 Å) was used as the x-ray source. Atomic force microscopy (AFM, SII SPI3800N-SPA400) observations were carried out to investigate the needle width and height for DSB-4Me microneedle crystals, and diameter and thickness for DADSB microdots.

For measurements of excitation density dependence of photoluminescence (PL) spectra for DSB-4Me microneedle crystals, a Ti:sapphire femtosecond pulsed laser with λ_{ex} = 400 nm, repetition rate of 1 kHz, and pulse width of 35-40 fs duration was used as an excitation source. A stripe-shaped excitation beam (2.5 mm×400 μm) was incident perpendicular to the needle crystal/KCl surface. The emitted light from the crystal edges was detected using a spectrometer (Roper Scientific, SP2156-300GK) and with a CCD camera (Princeton Instruments, ProEM512). In PL measurements for DADSB microdots, we used a neodymium (Nd):YAG laser (λ_{ex} = 355 nm, repetition rate of 1.2 kHz, pulse width of <1.1 ns) as an excitation source. The stripe-shaped beam (3.5 mm×570 μm) was incident with an

angle of approximately 45° to the microdot/KCl surface, and the light emission was detected from parallel direction to the substrate using a CCD spectrometer (Hamamatsu PMA-50).

3. Results and discussion

The molecular structure of DSB-4Me is shown in Fig. 1(a). Figures 1(b) and 1(c) show the fluorescence micrographs of DSB-4Me deposited without and with a shadow mask with pinholes. The pinhole contour is marked with a white dashed line in Fig. 1(c). In Fig. 1(c), the DSB-4Me needle crystals with a short length can be seen in the pinhole region, unlike conventional vacuum-deposited film without the mask as shown in Fig. 1(b), but longer needle crystals have been grown in the region covered with the mask.

Figure 1(d) represents the chemical structure of DADSB. The fluorescence micrographs of DADSB microdots fabricated without and with the pinhole mask are shown in Figs. 1(e) and 1(f), respectively. From the fluorescence images, we can see that DADSB microdots have 2-20 μm diameter, and they somewhere align in one direction (shown by arrows in Fig. 1(e)) along atomic steps of the KCl substrate surface. The growth feature of these isolated microdots is attributed to the impact of bulky peripheral groups in DADSB, and self-assembly via surface migration of the molecules during deposition at 180°C. In the case using the shadow mask as shown in Fig. 1(f) (pinhole position was marked with a white dashed line), the size and morphology remained seemingly unchanged as compared to the microdots fabricated by the conventional vapor deposition technique without the shadow mask shown in Fig. 1(e). This means that the mask-shadowing effect results in no dominant promotion in epitaxial growth for DADSB having bulky peripheral groups.

AFM images of representative DSB-4Me microneedle crystals and DADSB microdots are shown in Fig. 2. Figures 2(b) and 2(d) represent the cross-sectional profiles showing the height and width of DSB-4Me microneedle, and the diameter and thickness of DADSB microdots (measured positions are marked with lines in Figs. 2(a) and 2(c), respectively). In Fig. 2(b), the height (thickness) and width of the needle are 89 nm and 1.2 μm, respectively. In Fig. 2(d), the diameter/thickness of the two microdots are 3.94 μm/345 nm and 4.67 μm/367 nm.

Figure 3 shows the fluorescence micrographs without (a) and with ((b), (c)) a polarizer. The photographs of Figs. 3(b) and 3(c) were taken with the electric vector ***E*** set parallel to $[110]_{KCl}$ and $[-110]_{KCl}$ directions of the KCl substrate, respectively. As can be seen in Fig. 3, the DSB-4Me molecules grow into microneedle crystals epitaxially orienting in four

directions making ±60° with respect to the $[110]_{KCl}$ and $[-110]_{KCl}$. The epitaxial orientation originates in lying adsorption of the π-electronic backbone of DSB on the ionic row along $<110>_{KCl}$ as illustrated in Fig. 3(d).

Then we carried out XRD measurements to examine the crystal structure using single-crystal DSB-4Me prepared by the solution-grown method. The XRD analysis determined that the DSB-4Me molecules crystallized in orthorhombic form having P_{bca} space group with unit cell parameters a = 7.3327 Å, b = 5.8932 Å, c = 38.937 Å. Figure 4(a) shows the XRD pattern of DSB-4Me microneedle crystals. The diffraction peak at 2θ=23.6° corresponding to d-spacing of 0.377 nm indicates that the (200) plane of the DSB-4Me microneedle crystals is in contact parallel to the (001) face of the KCl substrate. Figure 4(b) shows the molecular alignment in the (200) plane of the DSB-4Me crystal. The molecular orientations projected on the bc plane in Fig. 4(b) indicates that the DSB-4Me molecules arrange with a tilt angle of 60° against b-axis of the crystal. This molecular orientation is in good agreement with the results of the oriented growth of DSB-4Me microneedle crystals shown in Fig. 3. An XRD pattern of the DADSB microdots transferred onto a glass substrate is shown in Fig. 4(c). The weak peak at 2θ=28.35° corresponds to the (200) reflection of the KCl substrate still remaining during the wet-transferring process. As a result, it is conceivable that the DADSB microdots have an amorphous structure since no diffraction peak was observed from the microdots.

We next investigated light amplification properties of the DSB-4Me microneedle crystals and DADSB microdots. Figure 5 shows excitation density dependences of their PL spectra. In Fig. 5(a) of the DSB-4Me microneedle crystals, three PL peaks located at 464 nm, 497 nm, and 532 nm correspond to the 0-1, 0-2, and 0-3 transitions from the lowest excited state to the vibronic levels of the ground state.[28)] The inset in Fig. 5(a) indicates the excitation density dependence of integrated PL intensity of the 0-1 band. Above an excitation density of 362 μJ/cm^2, spectral narrowing was observed at 464 nm corresponding to the 0-1 band. This gain-narrowed emission with a full width at half maximum (FWHM) of 8.5 nm at 799 μJ/cm^2 is ascribed to amplified spontaneous emission (ASE) in comparison to the weak fluorescence band with FWHM of 21.3 nm at 57 μJ/cm^2. This considerably high ASE threshold is probably caused by lower light confinement due to emission leakage from the surface of the needle crystals as well as unsuitable morphology leading to high-loss guided modes as is expected from Fig. 2(b). To reduce the threshold, further improvement of light

confinement to the crystal waveguide, reduction of propagation loss, and introduction of a resonator cavity are necessary.

Figure 5(b) and the inset show excitation density dependence of integrated PL intensity of the 0-1 band in the DADSB microdots. The change in PL spectra (spectral resolution of ~0.8 nm) demonstrates that light amplification is observed above an excitation threshold of 37 μJ/cm^2. This lower threshold in comparison to the DSB-4Me needle crystals can be attributed to stronger light confinement with lower propagation loss based on a whispering-gallery mode (WGM). In the high resolution PL spectra (spectral resolution of ~0.2 nm) shown in Fig. 5(c), emissions with mode structures were observed. Suppose that the refractive index n for DADSB is similar to other distyrylbenzene derivatives, the reported value n of 2.3-6.5[26, 27] allows a calculation of mode interval ΔE of 24-692 cm^{-1} for the DADSB microdots with 2-20 μm diameter, according to the relation of WGM lasing $\Delta E = hc/(n_{\mathrm{eff}} L)$,[30] where h is the Planck's constant, c is the speed of light, n_{eff} is the effective refractive index, and $L=\pi\phi$ (ϕ: diameter) is the round-trip distance within the microdot resonator. The ΔE value is not an equal interval even at 30 μJ/cm^2, showing that superposition of lasing from the microdots with different diameters. In order to clarify the mode interval in the lasing spectra, their spectra were Fourier transformed. Figure 5(d) represents the excitation density dependence of Fourier transformed spectra of PL spectra for DADSB microdots shown in Fig. 5(c). It was found from Fourier transformation (see Fig. 5(d)) of the lasing spectra that with increasing excitation density, additional oscillations with larger mode spacing were superimposed in the 0-1 band and the peak at 25cm^{-1} in the Fourier transformed spectra in Fig. 5(d) was obscured due to lasing from smaller microdots. Considering that the mode spacing of approximately 25 and 39 cm^{-1} at 30 μJ/cm^2 is almost consistent with the above ΔE values, the emissions with the mode structure from the DADSB microdots are attributed to WGM lasing.

4. Conclusions

We have fabricated DSB-4Me microneedle crystals and DADSB microdots by using mask-shadowing and conventional vapor deposition techniques. DSB-4Me vapor-deposited on $(001)_{\mathrm{KCl}}$ substrate grew into microneedle crystals epitaxially orienting in four directions making ±60° with respect to the $[110]_{\mathrm{KCl}}$ and $[-110]_{\mathrm{KCl}}$. The XRD measurements revealed that DSB-4Me molecules oriented in lying on the (001) surface of the KCl substrate. By contrast, DADSB vapor-deposited on $(001)_{\mathrm{KCl}}$ was self-assembled into amorphous

microdots since its bulky peripheral groups promote molecular migration on the KCl surface.

ASE was observed above an excitation density of 362 μJ/cm^2 for the DSB-4Me microneedle crystals while WGM lasing was observed above a lower threshold of 37 μJ/cm^2 for the DADSB microdots with higher waveguiding quality.

Acknowledgments

This work was supported by JSPS KAKENHI Grant Number 19H02172. The authors thank Mr. S. Katao, Nara Institute of Science and Technology for XRD measurements.

References

1) J. Liu, H. Zhang, H. Dong, L. Meng, L. Jiang, L. Jiang, Y. Wang, J. Yu, Y. Sun, W. Hu, and A. J. Heeger, Nat. Commun. **6**, 10032 (2015).
2) T. Kanagasekaran, H. Shimotani, K. Kasai, S. Onuki, R. D. Kavthe, R. Kumashiro, N. Hiroshiba, T. Jin, N. Asao, and K. Tanigaki, arXiv:1903.08869.
3) A. S. D. Sandanayaka, T. Matsushima, F. Bencheikh, S. Terakawa, W. J. Potscavage, Jr., C. Qin, T. Fujihara, K. Goushi, J.-C. Ribierre, and C. Adachi, Appl. Phys. Express **12**, 061010-1 (2019).
4) E. Wertz, L. Ferrier, D. D. Solnyshkov, R. Johne, D. Sanvitto, A. Lemaître, I. Sagnes, R. Grousson, A. V. Kavokin, P. Senellart, G. Malpuech, and J. Bloch, Nat. Phys. **6**, 860 (2010).
5) M. T. Hill and M. C. Gather, Nat. Photon. **8**, 908 (2014).
6) S. Chénais and S. Forget, Polym. Int. **61**, 390 (2012).
7) R. C. Somers, M. G. Bawendi, and D. G. Nocera, Chem. Soc. Rev. **36**, 579 (2007).
8) F. Vollmer and S. Arnold, Nat. Methods **5**, 591 (2008).
9) P. Liu, X. He, J. Ren, Q. Liao, J. Yao, and H. Fu, ACS Nano **11**, 5766 (2017).
10) Z. Yu, Y. Wu, L. Xiao, J. Chen, Q. Liao, J. Yao, and H. Fu, J. Am. Chem. Soc. **139**, 6376 (2017).
11) K. Torii, T. Higuchi, K. Mizuno, K. Bando, K. Yamashita, F. Sasaki, and H. Yanagi, ChemNanoMat **3**, 625 (2017).
12) C. Wei, S.-Y. Liu, C.-L. Zou, Y. Liu, J. Yao, and Y. S. Zhao, J. Am. Chem. Soc. **137**, 62 (2015).
13) C. Zhang, C.-L. Zou, Y. Yan, C. Wei, J.-M. Cui, F.-W. Sun, J. Yao, and Y. S. Zhao, Adv. Optical Mater. **1**, 357 (2013).
14) K. Bando, H. Fujii, K. Mizuno, K. Narushima, A. Miyazaki, F. Sasaki, S. Hotta, and H. Yanagi, ChemNanoMat **4**, 936 (2018).
15) S. Fujiwara, K. Bando, Y. Masumoto, F. Sasaki, S. Kobayashi, S. Haraichi, and S. Hotta, Appl. Phys. Lett. **91**, 021104 (2007).
16) H. Liu, X. Cao, Y. Wu, Q. Liao, A. J. Jiménez, F. Würthner, and H. Fu, Chem. Commun. **50**, 4620 (2014).
17) X. Wang, Q. Liao, X. Lu, H. Li, Z. Xu, and H. Fu, Scientific Reports **4**, 7011 (2014).
18) M. Schiek, F. Balzer, K. Al-Shamery, A. Lützen, and H.-G. Rubahn, J. Phys. Chem. C **113**, 9601 (2009).
19) H.-H. Fang, R. Ding, S.-Y. Lu, Y.-D. Yang, Q.-D. Chen, J. Feng, Y.-Z. Huang, and H.-B. Sun, Laser Photonics Rev. **2**, 281 (2013).

20) H. Mizuno, U Haku, Y. Marutani, A. Ishizumi, H. Yanagi, F. Sasaki, and S. Hotta, Adv. Mater. **24**, 5744 (2012).
21) T. Yamao, N. Sakamoto, S. Hotta, H. Mizuno, and H. Yanagi, Jpn. J. Appl. Phys. **51**, 11PD03-1 (2012).
22) H. Yanagi, N. Matsuoka, M. Kondo, M. Nagawa, and Y. Taniguchi, Langmuir **17**, 5491 (2001).
23) H. Yanagi, M. Kondo, N. Matsuoka, M. Nagawa, and Y. Taniguchi, Chem. Mater. **13**, 4800 (2001).
24) Z. Xu, Q. Liao, X. Wang, and H. Fu, Adv. Optical Mater. **2**, 1160 (2014).
25) J. Gierschner, Larry Lüer, B. Milián-Medina, D. Oelkrug, H.-J. Egelhaaf, J. Phys. Chem. Lett. **4**, 2686 (2013).
26) S. Varghese, S.-J. Yoon, S. Casado, R. C. Fischer, R. Wannemacher, S. Y. Park, and J. Gierschner, Adv. Optical Mater. **2**, 542 (2014).
27) X. Wang, Q. Liao, Q. Kong, Y. Zhang, Z. Xu, X. Lu, and H. Fu, Angew. Chem. Int. Ed. **53**, 5863 (2014).
28) R. Kabe, H. Nakanotani, T. Sakanoue, M. Yahiro, and C. Adachi, Adv. Mater. **21**, 4034 (2009).
29) H. Yanagi and T. Morikawa, Appl. Phys. Lett. **75**, 187 (1999).
30) X. Zhang, X. Zhang, J. Xu, X. Shan, J. Xu, and D. Yu, Opt. Lett. **34**, 2533 (2009).

Figure Captions

Fig. 1. (a) Molecular structure of DSB-4Me. Fluorescence micrographs of DSB-4Me deposited on $(001)_{KCl}$ kept at 100ºC without (b) and with (c) shadow-mask with pinholes. (d) Chemical structure of DADSB. Fluorescence micrographs of DADSB microdots deposited on $(001)_{KCl}$ kept at 180ºC without (e) and with (f) shadow-mask.

Fig. 2. AFM images of representative DSB-4Me microneedle crystals and DADSB microdots. Figures 2(b) and 2(d) indicate cross-sectional profiles showing height and width of the DSB-4Me microneedle crystal (marked with line in Fig. 2(a)), and diameter and thickness of the DADSB microdots (marked by line in Fig. 2(c)).

Fig. 3. Fluorescence micrographs of DSB-4Me microneedle crystals deposited on $(001)_{KCl}$ taken without (a) and with ((b), (c)) polarizer. Figures 3(b) and 3(c) were taken with electric vectors ***E*** set parallel to $[110]_{KCl}$ and $[-110]_{KCl}$ directions of KCl substrate, respectively. (d) Schematic diagram for epitaxial orientation showing lying adsorption of DSB molecules on ionic row along $<110>_{KCl}$.

Fig. 4. (a) XRD pattern of the DSB-4Me microneedle crystals. (b) Schematic representation of molecular alignment in the (200) plane of DSB-4Me crystal. (c) XRD pattern of DADSB microdots transferred onto a glass substrate.

Fig. 5. Excitation density dependence of PL spectra of DSB-4Me microneedle crystals (a) and DADSB microdots capped with MgF_2 layer (b, c). The inset in Figs. 5(a) and 5(b) indicate excitation density dependences of integrated PL intensity of the 0-1 band. Figure 5(c) shows high-resolution PL spectra of the DADSB microdots. (d) Excitation density dependence of Fourier transformed spectra of PL spectra for DADSB microdots in Fig. 5(c).

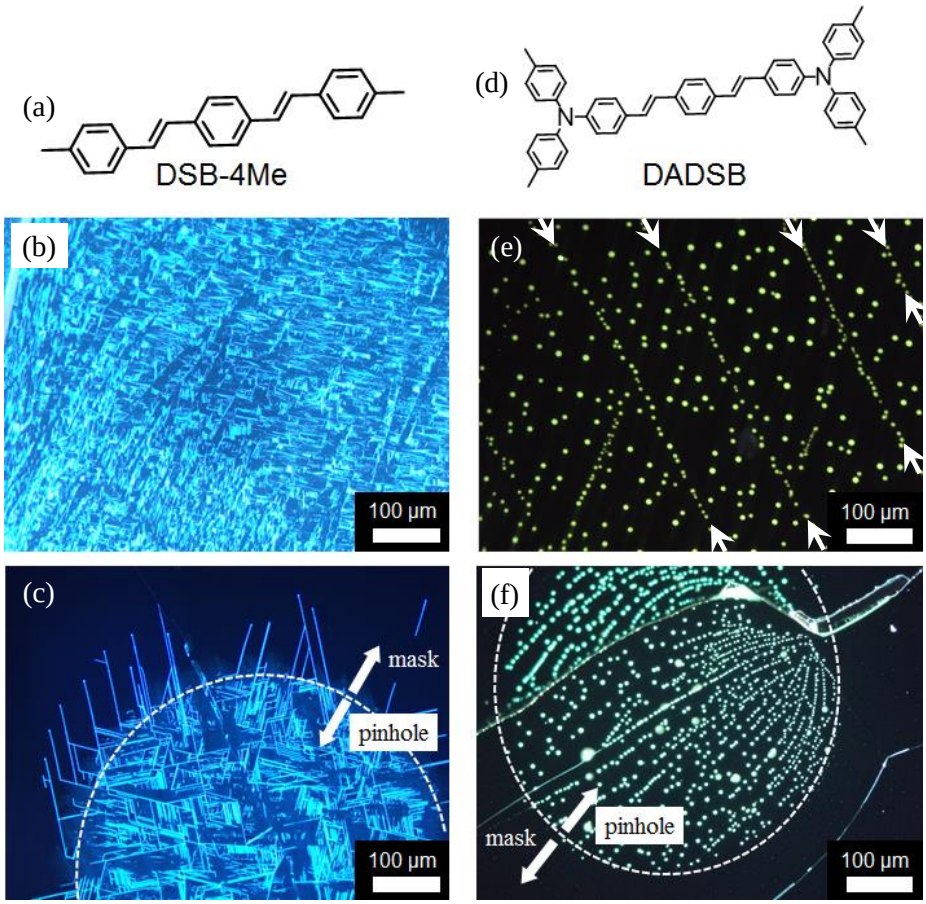
(a)
DSB-4Me
(d)
DADSB
(b)
100 μm
(e)
100 μm
(c)
mask
pinhole
100 μm
(f)
mask
pinhole
100 μm

Fig.1.

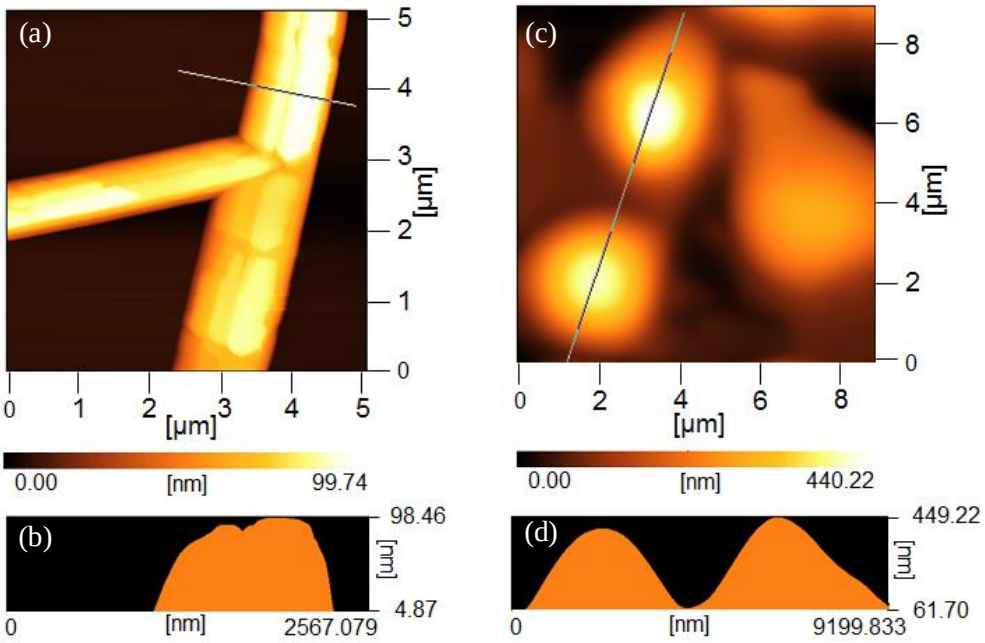
(a)
5
4
3
2
1
0
[µm]
0 1 2 3 4 5
[µm]
0.00 [nm] 99.74
(b)
98.46
[nm]
4.87
0 [nm] 2567.079
(c)
8
6
4
2
0
[µm]
0 2 4 6 8
[µm]
0.00 [nm] 440.22
(d)
449.22
[nm]
61.70
0 [nm] 9199.833

Fig. 2.

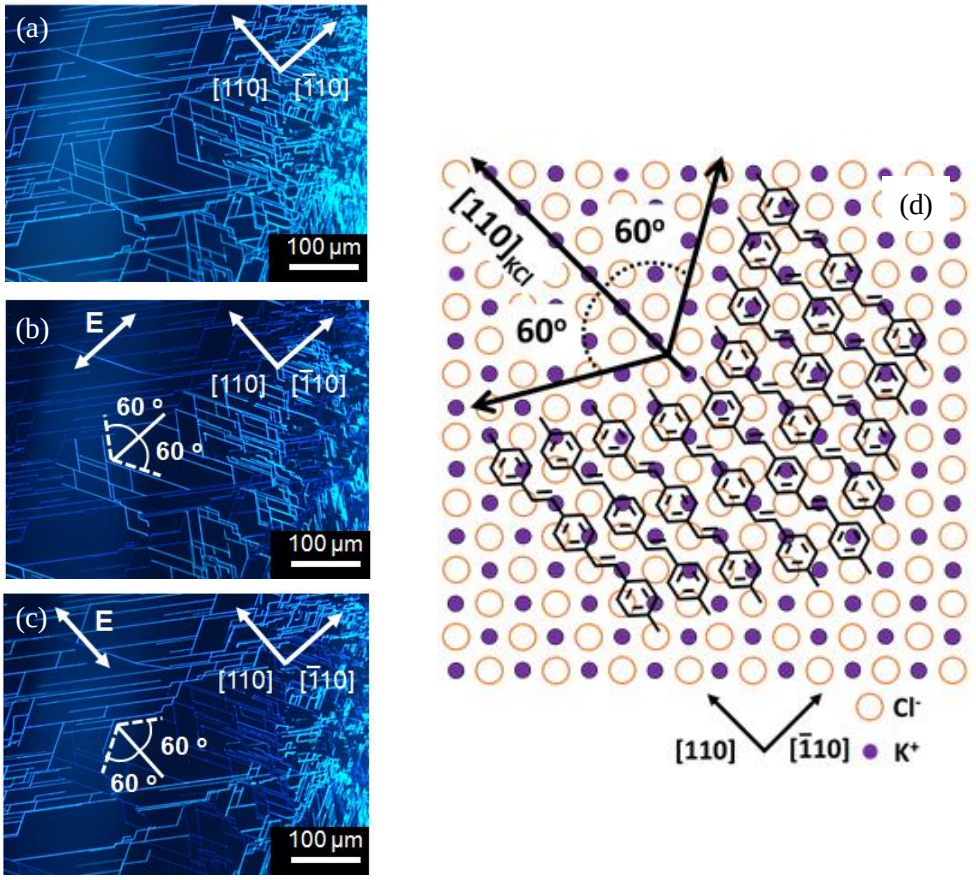
(a)
[110]
[$\bar{1}$10]
100 μm
(b)
E
[110]
[$\bar{1}$10]
60 °
60 °
100 μm
(c)
E
[110]
[$\bar{1}$10]
60 °
60 °
100 μm
(d)
[110]KCl
60°
60°
[110]
[$\bar{1}$10]
Cl-
K+

Fig. 3.

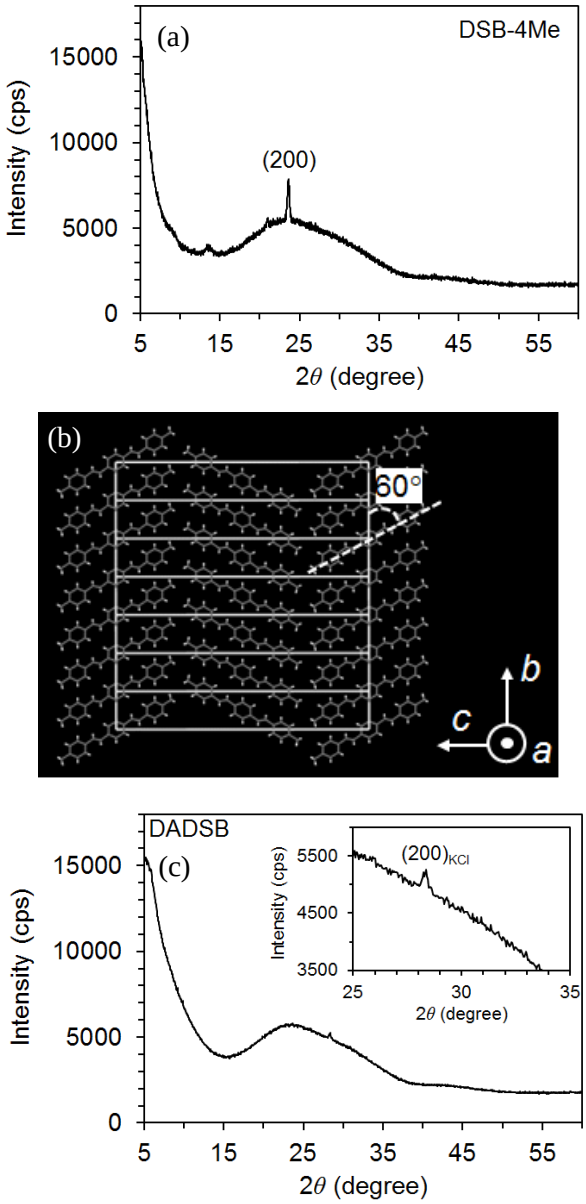
(a)
DSB-4Me
(200)
Intensity (cps)
2θ (degree)
(b)
60°
b
c
a
DADSB
(c)
(200)KCl
Intensity (cps)
2θ (degree)

Fig. 4.

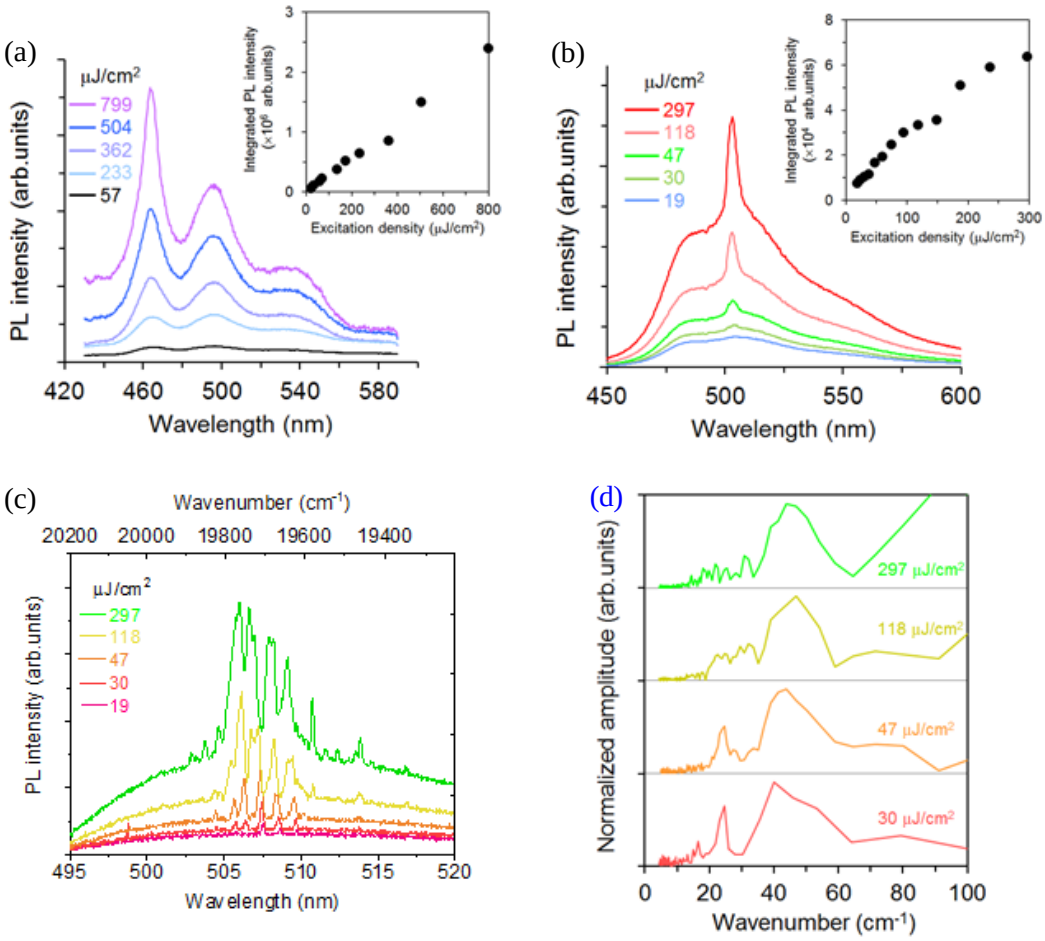
(a)
μJ/cm²
799
504
362
233
57
PL intensity (arb.units)
Wavelength (nm)
Integrated PL intensity (×10⁴ arb.units)
Excitation density (μJ/cm²)
(b)
μJ/cm²
297
118
47
30
19
PL intensity (arb.units)
Wavelength (nm)
Integrated PL intensity (×10⁴ arb.units)
Excitation density (μJ/cm²)
(c)
Wavenumber (cm⁻¹)
μJ/cm²
297
118
47
30
19
PL intensity (arb.units)
Wavelength (nm)
(d)
297 μJ/cm²
118 μJ/cm²
47 μJ/cm²
30 μJ/cm²
Normalized amplitude (arb.units)
Wavenumber (cm⁻¹)

Fig. 5.